Chinese Journal of Chemical Engineering 89 (2026) 277–292

Contents lists available at ScienceDirect

Chinese Journal of Chemical Engineering

journal homepage: www.elsevier.com/locate/CJChE

Full Length Article

Electrochemical oscillatory behaviour of manganese ions and its square wave modulation

Jiaxing Li [1], Chunbiao Li [2], Jie Yang [1], Zhihao Wu [1], Qian Zhang [1], Guocan Zheng [1], Zuohua Liu [1, 3, *], Changyuan Tao [1, 3]

[1] School of Chemistry and Chemical Engineering, Chongqing University, Chongqing 400044, China
[3] State Key Laboratory of Coal Mine Disaster Dynamics and Control, Chongqing 400044, China
[2] School of Artificial Intelligence, Nanjing University of Information Science and Technology, Nanjing 210044, China

ARTICLE INFO

Article history:
Received 16 April 2025
Received in revised form
31 May 2025
Accepted 28 July 2025
Available online 11 November 2025

Keywords:
Manganese electrolysis
Electrochemical oscillation
Square wave circuit
Energy reduction

ABSTRACT

In manganese electrolysis, electrochemical oscillations and manganese dendrite growth are typical nonlinear phenomena critical for energy consumption reduction. Nonetheless, existing research lacks a deep understanding of their underlying mechanisms. In this study, we systematically explored the evolution of anode electrochemical oscillations during manganese electrolysis and designed a square wave circuit to effectively suppress oscillations and dendrite growth while reducing energy consumption. A novel four-dimensional differential equation was introduced to explore the internal dynamic mechanisms of typical nonlinear behaviors. The experimental results showed that while the evolutionary patterns of current and potential oscillation signals were consistent, their waveform directions were opposite. The square wave current effectively suppressed both electrochemical oscillations and the growth of manganese dendrites. Furthermore, compared to direct current electrolysis, the square wave current improved the current efficiency by 3.6% and reduced the energy consumption by 0.32 $kW \cdot h \cdot kg^{-1}$.

1. Introduction

In nature, numerous phenomena that seem random and unpredictable may actually be driven by simple rules and complex nonlinear interactions, including variations in meteorological systems, the evolution of population dynamics, geological changes, and other intricate phenomena [1–3]. The examination of these complex phenomena has facilitated the formation and development of chaos theory. Chaos is a type of complex dynamical behavior inherent in nonlinear dynamical systems, exhibiting an inherent degree of randomness [4]. The essence of chaos control theory lies in regulating external conditions to control these intricate systems [5,6].

Chaotic systems are broadly classified into discrete-time maps and continuous-time dynamical systems, with the latter being more prevalent in modeling processes due to their differential equation-based formalism. Due to their simple structure and limited variables, low-dimensional chaotic mappings offer weak confidentiality in image encryption. Consequently, researchers are shifting towards high-dimensional chaotic mappings to bolster the system's security against malicious attacks [7,8]. As research progresses, three-dimensional continuous chaotic systems have increasingly become a significant area of focus. Simple three-dimensional continuous chaotic systems such as Lorenz were the first chaotic dynamical systems discovered [9]. With further research, systems like Rössler, Chua, Colpitts, Rikitake, and others have been proposed successively [10–12]. To delve into higher-dimensional chaotic systems and differentiate them from conventional three-dimensional chaotic systems, hyperchaotic systems have been proposed. These systems are characterized by having at least two positive Lyapunov exponents, such as multi-vortex four-dimensional hyperchaotic systems and five-dimensional Sprott B hyperchaotic systems [13,14]. Wang *et al.* [15] designed a four-dimensional fractional-order hyperchaotic system with coexisting attractors, and analyzed the stability of the system and the conditions for the existence of a Hopf bifurcation. Xiu *et al.* [16] designed a novel 5D memristive CNN hyperchaotic system, and verified the physical realizability of the chaotic behavior in the cellular neural network model with memristors.

* Corresponding author.
E-mail address: liuzuohua@cqu.edu.cn (Z. Liu).

https://doi.org/10.1016/j.cjche.2025.07.022

Table 1
Comparison of the research presented in this paper with existing literature.

Source	SW current	System analysis	Oscillation analysis	Application areas
Yang *et al.* [34]	No	Yes	No	Electrolytic industry
Xie *et al.* [35]	No	No	Yes	
Hakimi *et al.* [36]	Yes	No	No	Electrode material
Jain *et al.* [37]	Yes	No	No	Copper nanoparticle
Hansen *et al.* [38]	Yes	No	No	Neuron
Gao *et al.* [39]	Yes	No	No	Wastewater treatment
Ruiz *et al.* [40]	Yes	Yes	No	Nonlinear circuit
Wan *et al.* [41]	Yes	Yes	No	Hopfield neural network
Jafari *et al.* [42]	Yes	No	No	Liquid–liquid extraction
Gong *et al.* [43]	Yes	No	No	Demulsification
This work	Yes	Yes	Yes	Electrolytic industry

Chaos theory has seen increasing application across various fields, achieving good effects in disciplines such as economics, chemistry, cryptography, and ecology [17–21], but its application in the field of manganese electrolysis is relatively scarce. The manganese electrolysis industry faces numerous difficulties and challenges, including the recycling of anode slime and manganese slag [22–25]. However, the main issues in manganese electrodeposition are low current efficiency, high cell voltage, and high energy consumption. To address these challenges, researchers have focused on optimizing electrode materials and electrolyser structures. Additionally, emphasis is placed on strategies for additives, especially borrowing from the battery industry and other fields to develop new additives [26–33]. Although additive-based strategies and electrode modifications have partially mitigated energy consumption issues, these approaches often fail to address persistent challenges such as dendrite growth and electrochemical oscillations. Furthermore, current research remains insufficient in unraveling their underlying mechanisms. Consequently, there is an urgent need to develop viable and effective methods to address these challenges, thereby promoting the sustainable development of the electrolytic manganese industry. A comparison of the research in this paper with existing literature is shown in Table 1.

To further elucidate the evolution of electrochemical oscillations in manganese metal electrodeposition, this paper investigated the evolution of anode electrochemical oscillations and their mechanisms in electrolytic manganese, and designed a square wave (SW) circuit to effectively suppress oscillations and dendrite growth while reducing energy consumption (Fig. S1, Supplementary Material). Furthermore, a novel four-dimensional differential equation was proposed to analyze the potential kinetic mechanisms of electrochemical oscillations from a kinetic perspective. The experimental results indicated that the current and potential oscillation signals exhibited consistent evolution processes but with opposite waveforms, and the SW current effectively suppressed electrochemical oscillations. This research not only offers a fresh direction for reducing energy consumption in the manganese electrolysis industry but also serves as a theoretical and technical reference for improving processes in other electrolysis industries.

2. Materials and Methods

2.1. Reagents and materials

All reagents for the experiments were analytically pure reagents without additional purification treatment. The components and concentrations of the electrolyte were $MnSO_4$ (92 $g\cdot L^{-1}$), $(NH_4)_2SO_4$ (120 $g\cdot L^{-1}$), and SeO_2 (30 $mg\cdot L^{-1}$). Ammonia was added to the electrolyte to maintain pH 7. In the simulated industrial electrodeposition experiments, a 304 stainless steel plate was used as the cathode and a lead-based quaternary alloy ($PbSn_{0.4}Ag_{0.014}Sb_{0.014}$) was used as the anode, with a plate spacing of (3.7 ± 0.1) cm and a width of (2 ± 0.1) cm. Manganese electrolysis reacts at 40 °C. Ultrapure water was prepared by a water purification system (HMC-WS10, Human Company, Korea).

2.2. Electrochemical testing and experimental equipment

Fig. 1 shows the experimental setup for electrochemical oscillations, which contains a power supply (SPD3303X-C, SIGLENT, China), a circuit board (signal generating module, the SW circuit schematic is shown in Fig. S2), an oscilloscope (SDS1102X-C, SIGLENT, China), a current control module, a power amplifier (ATA101B, Aigtek, China), a multimeter (Acquisition of cell voltage and electrical signals), electrolytic cell, an electrochemical workstation (CHI660E, Shanghai Chenhua, China). Electrochemical oscillation experiment was carried out using a three-electrode system, in which the counter electrode was a platinum electrode (1 cm × 1 cm in size and about 1 mm in thickness), the reference electrode was a saturated calomel electrode, and the working electrode was a conical quaternary alloy of $PbSn_{0.4}Ag_{0.014}Sb_{0.014}$ (diameter about 3 mm). The spacing of the working electrode, the reference electrode, and the counter electrode was (1.1 ± 0.05) cm, and the external power supply was used to regulate the anodic potential. The open-circuit-time mode (OCPT, sampling interval 0.006 s) was used for oscillation. The anode potential signals were acquired by the electrochemical workstation and the signal processing was performed with a low-pass filter (0.5 Hz) to filter the noise.

2.3. Characterization method

The main components of the anode products were tested by XRD (EMPYREAN, PANalytical B.V, The Netherlands). The microstructure of the anode and cathode was tested by SEM-Mapping (TESCAN MIRA LMS, TESCAN, The Czech Republic, and Zeiss Gemini Sigma 300, Carl Zeiss AG, The Federal Republic of Germany). In order to analyze the chemical composition of the anode products, the anode products were analyzed using Raman spectroscopy (LabRAM HR Evolution, HORIBA Jobin Yvon S.A.S, The French Republic) test at 532 nm.

2.4. Calculation of current efficiency and energy consumption

The current efficiency (ratio of effective current to total current used for manganese electrodeposition) was calculated using Eq. (1).

$$\eta_c = \frac{\Delta M_c}{E_{Mn} I_c \Delta t} \tag{1}$$

where η_c (%) is the current efficiency, $\Delta M_c/\Delta t$ ($g\cdot s^{-1}$) is the mass gain of the cathode mass at the time interval Δt. I_c is the current (A), and E_{Mn} is the electrochemical equivalent, equal to 1.025 $g\cdot(A\cdot h)^{-1}$.

Calculation of specific energy consumption for manganese electrodeposition using Eq. (2) [44].

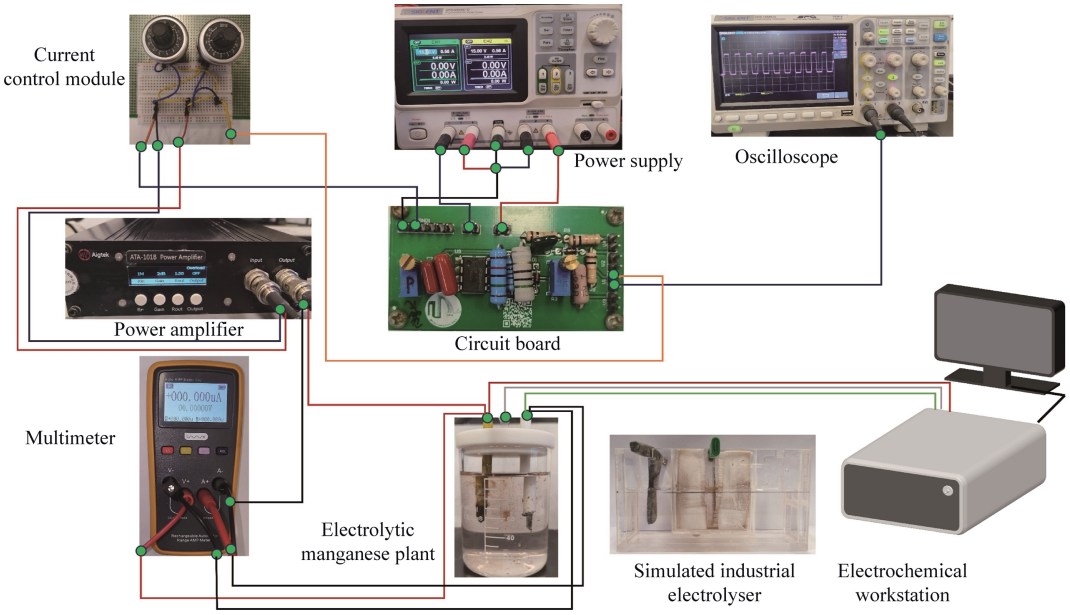

Fig. 1. Schematic diagram of electrochemical experimental device.

$$W_{Mn} = \frac{CV \times 1000}{E_{Mn} \times \eta_c} \quad (2)$$

where W_{Mn} is the unit energy consumption of manganese metal ($kW \cdot h \cdot t^{-1}$) and CV is the cell voltage (V). To avoid experimental errors, the average current and average voltage of the whole electrodeposition process collected by the current-voltage analyzer were used to fit this paper.

3. Electrochemical Oscillations

3.1. Transient state

Electrolysis of manganese metal occurs in an open, flowing system, which is a typical nonlinear process deviating from equilibrium [45,46]. The anode exhibits abundant nonlinear behavior during electrolysis. To investigate the process and underlying causes of anodic electrochemical oscillation generation, constant current electrolysis was employed in manganese electrolysis experiments. Anodic potential oscillation data were collected using the chronopotentiometry, resulting in Fig. 2(a). To ensure the reliability of the results, the experiment was repeated four times to obtain Fig. 2(b). The figure shows that the generation of anodic potential oscillation is a gradual process, progressing through a stationary phase (where the potential remains essentially constant), a transitional period (where the potential begins to oscillate with small amplitude and frequency), and an oscillatory period (where the potential continuously oscillates, with the amplitude increasing over time). In addition, analogous oscillatory states are observed during neuronal oscillations [47,48]. The anodic mud undergoes three distinct stages: formation, envelopment, and detachment. This process is analogous to the process involved in the formation of electrochemical oscillations (Fig. 2(c)). Furthermore, studies have revealed a certain correlation between the formation of anode slime and anodic electrochemical oscillations [49].

3.2. Cyclic voltammetry (CV)

To investigate the impact of anode potential on the formation of electrochemical oscillations, cyclic voltammetry tests were conducted using the electrochemical setup shown in Fig. 3(a). As depicted in Fig. 3(b), no oscillation peaks were observed during the first forward scan. However, oscillation peaks emerged during the reverse scan, and their amplitude and frequency gradually decreased and disappeared as the voltage decreased. In the second cycle, oscillation peaks appeared in both the forward and reverse scans, suggesting that the anode might be fully covered by anode slime. Repeated CV tests were conducted to observe the changes in electrochemical oscillations following the complete formation of anodic slime. After the anodic slime was fully formed, the frequency and amplitude of the anodic current oscillations increased with the anodic potential (Fig. 3(c)–(d)). These results were consistent with the scanning results observed in the second cycle of Fig. 3(b). This indicates that both the amplitude and frequency of anodic current oscillations are positively correlated with the anodic potential, meaning that the input of external energy can influence the reaction rate of the anode, and changes in voltage can accelerate or decelerate the formation of current oscillations.

3.3. Potential oscillation

3.3.1. The influence of current intensity on potential oscillation

To explore the influence of anodic current on anodic potential oscillations, electrolytic manganese experiments were conducted under various current conditions. As evident from Fig. 4(a), the results of the three repeated experiments were largely consistent. The second set of these repetitions, which exhibited greater stability, was selected for further analysis. As shown in Fig. 4(b), with an increase in current, both the amplitude and frequency of anodic potential oscillations exhibit an upward trend, and the overall potential level of the

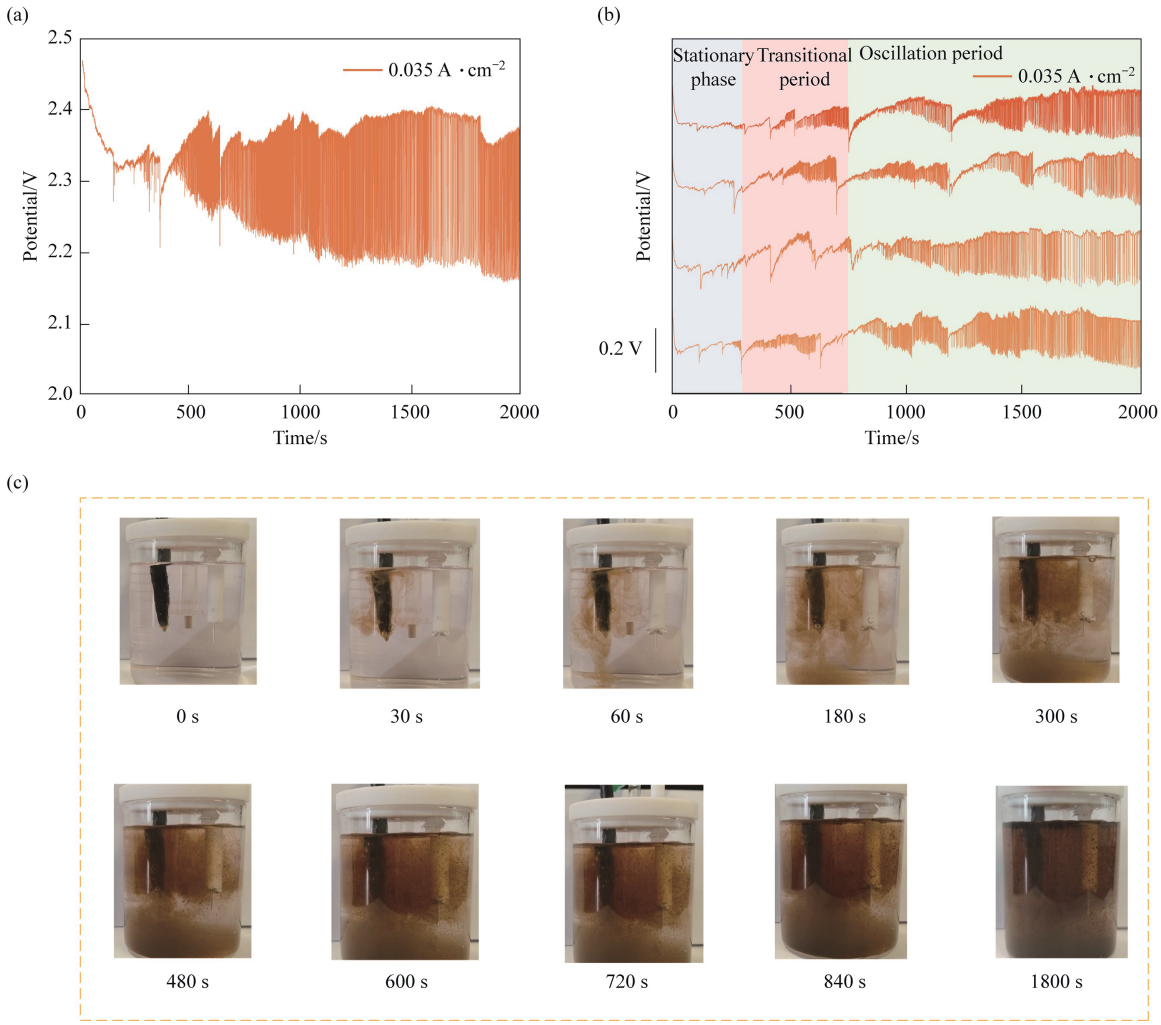

Fig. 2. Experimental results of anodic potential oscillation with a current intensity of 0.035 A·cm^{-2} and pH 7. (a) The first experiment, (b) repeated four experiments under the same conditions, (c) the formation process of anode slime.

oscillations shifted upwards. These observations indicate that the input of external energy accelerates the reaction rate at the anode. At a current of 0.01 A no potential oscillation occurs at the anode, with the potential remaining constant. When the current increased to 0.03 A, potential oscillation occurs at the anode. It is demonstrated that the occurrence of potential oscillations at the anode requires appropriate conditions, and that variations in anodic current can either promote or inhibit these oscillations.

3.3.2. Phase space reconstruction of potential oscillation delay mapping (excluding transient)

To further analyze the anode potential signal and investigate the impact of varying currents on the anode's response, phase space reconstruction of the signal was conducted. Phase space reconstruction [50] is a scientific method that assesses the presence of nonlinear relationships within a signal and is extensively utilized in ecosystems, climate systems, biological systems, and engineering systems [51–53]. Consequently, the electrochemical oscillatory signals generated during the electrolysis of manganese metal were subjected to phase space reconstruction.

As shown in Fig. 5(a), at the same current density, the graph after phase space reconstruction of the anode potential signal gradually unfolds and changes shape as the delay time τ increases. Comparing Fig. 5(a) and (b), it is evident that the shape resulting from phase space reconstruction remains largely unchanged at the same delay time. As current density increases, the initial potential shifts from 2.2 V to 2.3 V, and concurrently, the entire graph is positionally offset towards the upper right. The structure of the attractor obtained through phase space reconstruction under different currents is essentially the same, with only the position being shifted. This suggests that the increase in current did not initiate a novel electrochemical reaction, but only served to intensify the reaction process.

3.4. Current oscillation

3.4.1. The influence of voltage intensity on current oscillation

Based on previous findings, it is established that the anode not only exhibits potential oscillations but also generates current oscillations (Figs. 2 and 3). In order to further explore the formation process of current oscillations and the effect of different potentials on current oscillations, manganese electrolysis

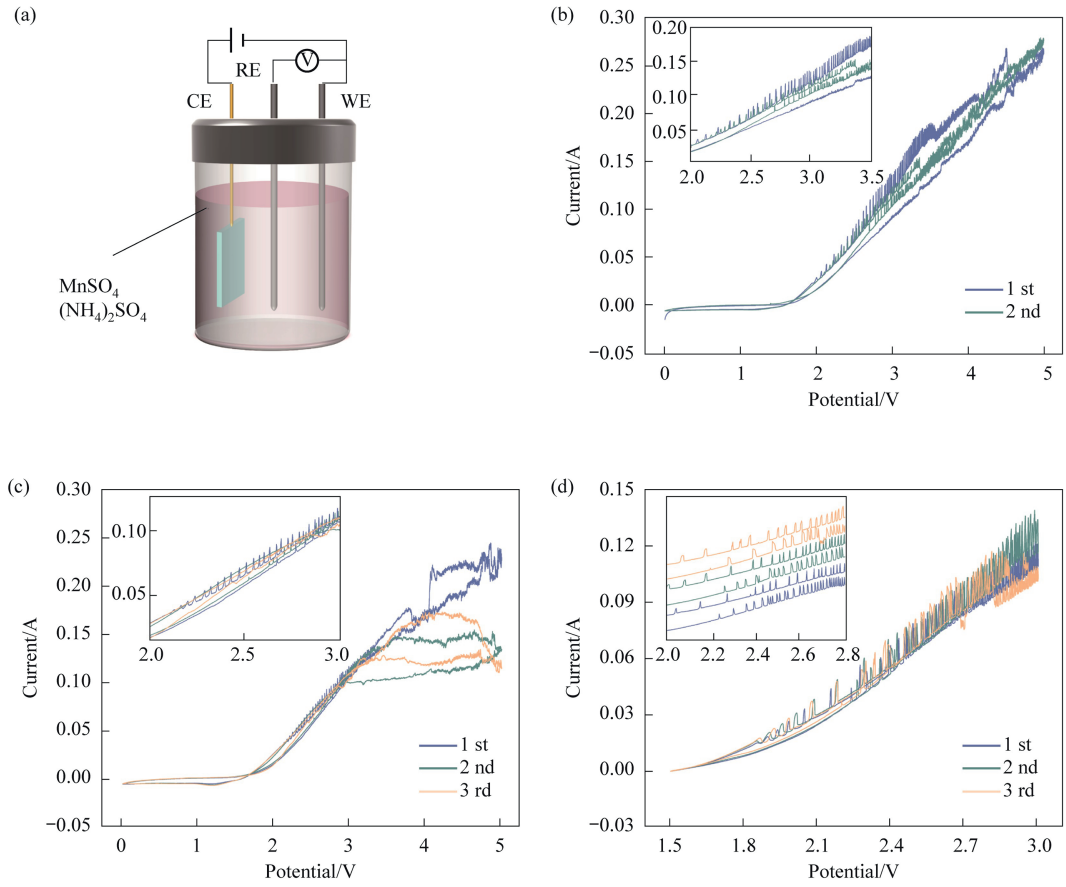

Fig. 3. Cyclic voltammetry scan results with a starting scanning direction of anode and a sample interval of 0.001 V. (a) Schematic diagram of electrochemical test, (b) CV results before and after anode slime formation (scanning speed: 0.005 $V \cdot s^{-1}$), (c) CV results of repeated experiments after the formation of porous anode (scanning speed: 0.005 $V \cdot s^{-1}$), (d) CV results of repeated experiments after the formation of porous anode (scanning speed: 0.002 $V \cdot s^{-1}$).

experiments were conducted at various potentials, with concurrent collection of anode current signals. To obtain reliable experimental results, the experiment was repeated three times at the same voltage (Fig. 4(c)). The results of the second experiment were selected to obtain Fig. 4(d). As depicted in Fig. 4(d), at a potential of 2.0 V, the anode does not exhibit current oscillations, and the current remains stable. As the potential gradually increases, the anode begins to generate current oscillations with small frequency and amplitude. When the potential reaches 2.6 V, both the frequency and amplitude of the anode current oscillations increase, and the overall current oscillations shift upwards. It is demonstrated that the onset of current oscillations is a gradual process, and there exists a close correlation between the generation of current oscillations and the formation of anodic slime. Furthermore, anodic current oscillations occur under specific conditions, and changes in potential can either promote or inhibit them. This is analogous to the impact of different currents on potential oscillations.

3.4.2. Phase space reconstruction of current oscillation delay mapping (excluding transient)

To further analyze the anode current signal and investigate the impact of varying potentials on the anodic reaction, phase space reconstruction of the anode current signal was conducted. As shown in Fig. 5(c), with an increase in delay time, the attractor shape progressively unfolds, revealing a more regular structure and better showcasing the information within the current oscillations. A comparable change is evident in Fig. 5(a). Upon comparing Fig. 5(c) with Fig. 5(d), it is noted that as the potential increases, the initial current shifts from 0.100 A to 0.123 A, and the current oscillation attractor is observed to shift towards the upper right. A similar pattern is also seen between Fig. 5(a) and (b). The results of the phase space reconstruction analysis indicate that the anode current signal and the potential signal exhibit similar variation trends. Notably, the chaotic attractor structure formed by the phase space reconstruction of the current and potential oscillation signals appears symmetric about the line $y = x$, implying a certain degree of correlation between the current and potential signals.

4. Chaotic System Design

4.1. System attractor

To systematically investigate the evolutionary mechanisms of electrochemical oscillations, we propose a novel four-dimensional differential equation based on the Rössler. The classical three-dimensional Rössler system (Eq. (S1) in Supplementary Material) manifests chaotic characteristics in its phase space (Fig. S5(a)–(c)). However, it demonstrates critical limitations when modeling electrochemical oscillatory behaviors. Specifically:

(1) Mismatch of described objects: As the parameter a increases, the waveform of y exhibits gradual transformations,

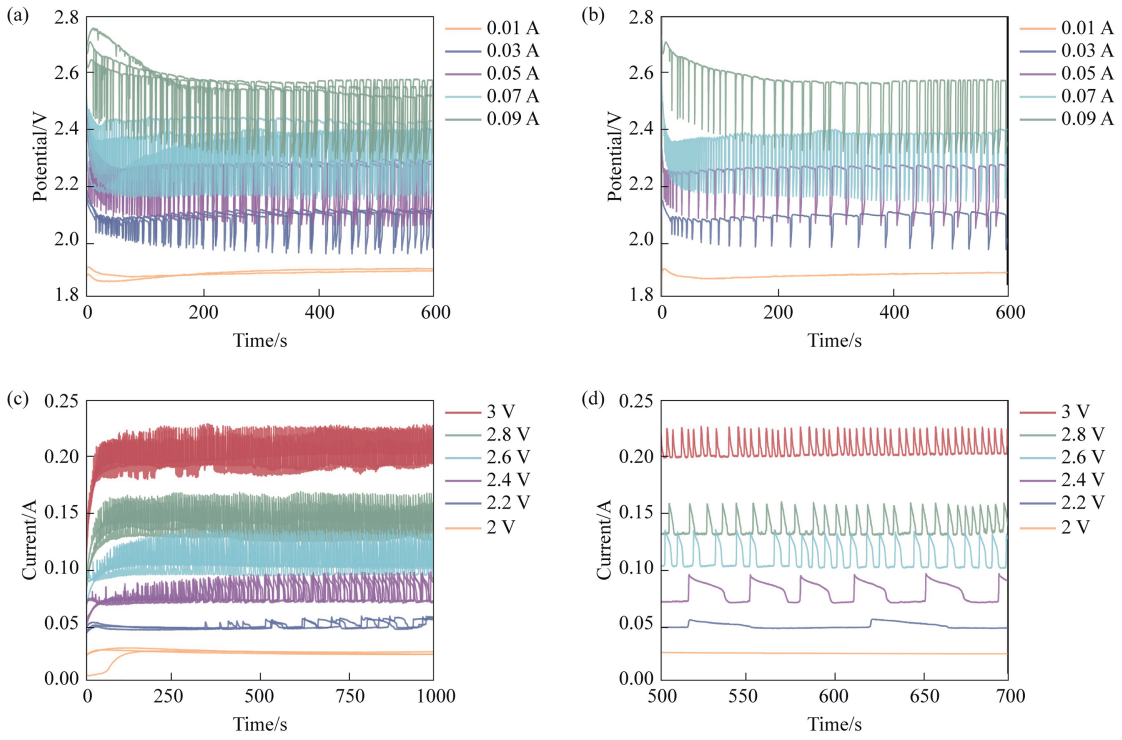

Fig. 4. Electrochemical oscillations under different conditions with cathode area of 2 cm^2, (a) summary chart of all data on potential oscillation, (b) results of the second experiment data in (a), (c) summary of all current oscillation data, (d) the local current oscillation amplification diagram of the second experiment in (c).

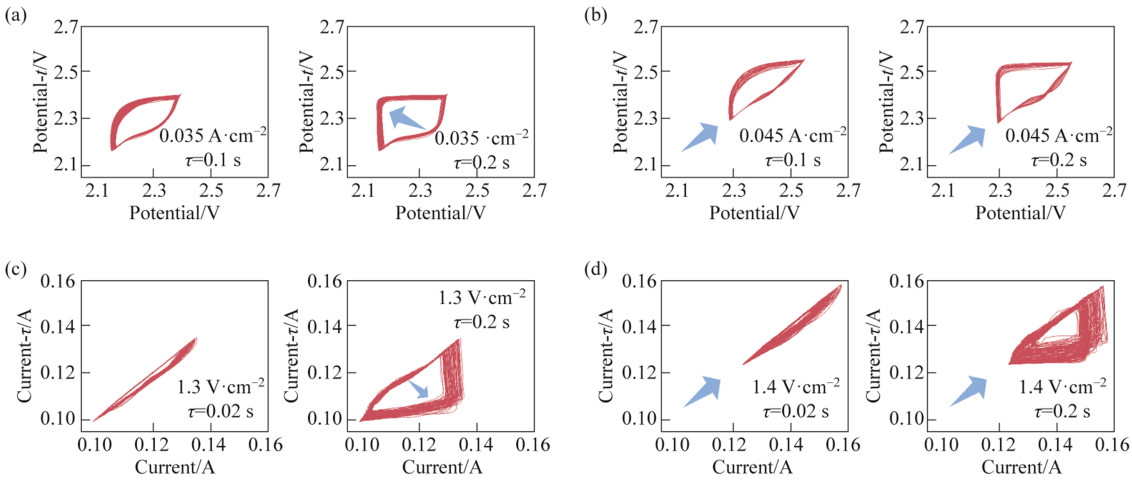

Fig. 5. Phase space reconstruction of anode electrical signals at different delay times. (a) Potential signal at a current density of 0.035 A·cm^{-2}, (b) potential signal at a current density of 0.045 A·cm^{-2}, (c) current signal at a potential of 1.3 V·cm^{-2}, (d) current signal at a potential of 1.4 V·cm^{-2}.

but it fails to consistently align with the waveform observed in experimental outcomes (Fig. S5(d)).

(2) Asymptotic behavior inadequacy: While z evolves from periodic to chaotic states at $c = 4$–10, it fail to describe the experimentally observed progressive behaviour of electrochemical oscillations when $c > 10$ (Fig. S5(e)).

(3) Inverse bifurcation behavior: Increasing parameter b drives z from chaos to periodicity, contradicting the electrochemical oscillation trends (Fig. S5(f)).

These limitations stem from the intrinsic simplicity of the three-dimensional Rössler system, which inadequately describes high-

dimensional nonlinear interactions. Therefore, introducing a higher-dimensional chaotic system becomes imperative to accurately characterize the complex dynamics of electrochemical oscillations.

To construct higher-dimensional chaotic systems, nonlinear terms are typically introduced into the three-dimensional framework. As shown in Eq. (3), the extended Rössler system incorporates: (1) a nonlinear coupling term $z(-k_1+k_2|w|)$ in the first dimension, where $|w|$ interacts dynamically with z; (2) a linear term $4(n-1)z$ in the third dimension to regulate the growth or decay rate of z; and (3) a linear feedback coupling between w and z in the fourth dimension, enhancing the interplay between variables.

The novel established four-dimensional Rössler-like chaotic system is presented in Eq. (3).

$$\begin{cases} \dot{x} = -y - z(-k_1 + k_2|w|) \\ \dot{y} = x + ay \\ \dot{z} = b + xz - cz - 4(n-1)z \\ \dot{w} = 1 + 23(7-n)^2(z-(w-n)) \end{cases} \tag{3}$$

where a, b, c, k_1, k_2, and n are the system parameters, and the system is period when $a = 0.1$, $b = 0.1$, $c = 2.2$, $k_1 = 0.3$, $k_2 = 3.2$, $n = 1$.

A novel four-dimensional chaotic system (3) is obtained by introducing a state variable w based on the improvement of the Rössler system. The phase trajectory diagram Fig. 6 of system (3) is obtained after computation by MATLAB software. The dissipativity of Eq. (3) is analyzed to obtain the following results:

$$\nabla V = \frac{\partial \dot{x}}{\partial x} + \frac{\partial \dot{y}}{\partial y} + \frac{\partial \dot{z}}{\partial z} + \frac{\partial \dot{w}}{\partial w} = x - 830.1 \tag{4}$$

when $x < 830.1$, $\nabla V < 0$, indicating that system (3) is stable. As time approaches infinity, each volume element containing a system trajectory shrinks exponentially towards 0 at a rate of $x - 830.1$. Consequently, all system trajectories converge asymptotically to a fixed attractor.

To find the equilibrium point of the system where the right-hand side of Eq. (3) equals zero, the following equation is derived:

Table 2
Eigenvalues for each equilibrium and corresponding equilibrium types.

λ	S_1	S_2
λ_1	−828	−828.0184
λ_2	−2.1292	−0.0118 + 6.1441i
λ_3	0.0216 + 1.0096i	−0.0118 − 6.1441i
λ_4	0.0216 − 1.0096i	0.0961
Equilibrium stability	Unstable saddle focus	Unstable saddle focus

$$\begin{cases} -y - z(-k_1 + k_2|w|) = 0 \\ x + ay = 0 \\ b + xz - cz - 4(n-1)z = 0 \\ 1 + 23(7-n)^2(z-(w-n)) = 0 \end{cases} \tag{5}$$

Solving Eq. (5) yields two equilibrium points $S_1 = (0.0140, -0.1397, 0.0458, 1.0470)$, $S_2 = (2.1541, -21.5414, 2.1802, 3.1814)$. The jacobi matrix of system (3) at the equilibrium point is as follows:

$$\boldsymbol{J} = \begin{bmatrix} 0 & -1 & k_1 - k_2|w| & -k_2 z \\ 1 & a & 0 & 0 \\ z & 0 & x - c - 4n + 4 & 0 \\ 0 & 0 & 23(7-n)^2 & -23(7-n)^2 \end{bmatrix} \tag{6}$$

The roots of the characteristic equations corresponding to the two equilibrium points are calculated as shown in Table 2. The type of equilibrium point is determined by the roots of the characteristic equation [54,55].

4.2. Simultaneous adjustment of signal amplitude, frequency, and offset boosting

In order to explore the effect of parameter n on the state variable w, the time series plot of w is obtained by MATLAB calculation. As illustrated in Fig. 7(a), as the parameter n varies from 0.6 to 1.6, the amplitude and the offset of the w signal are

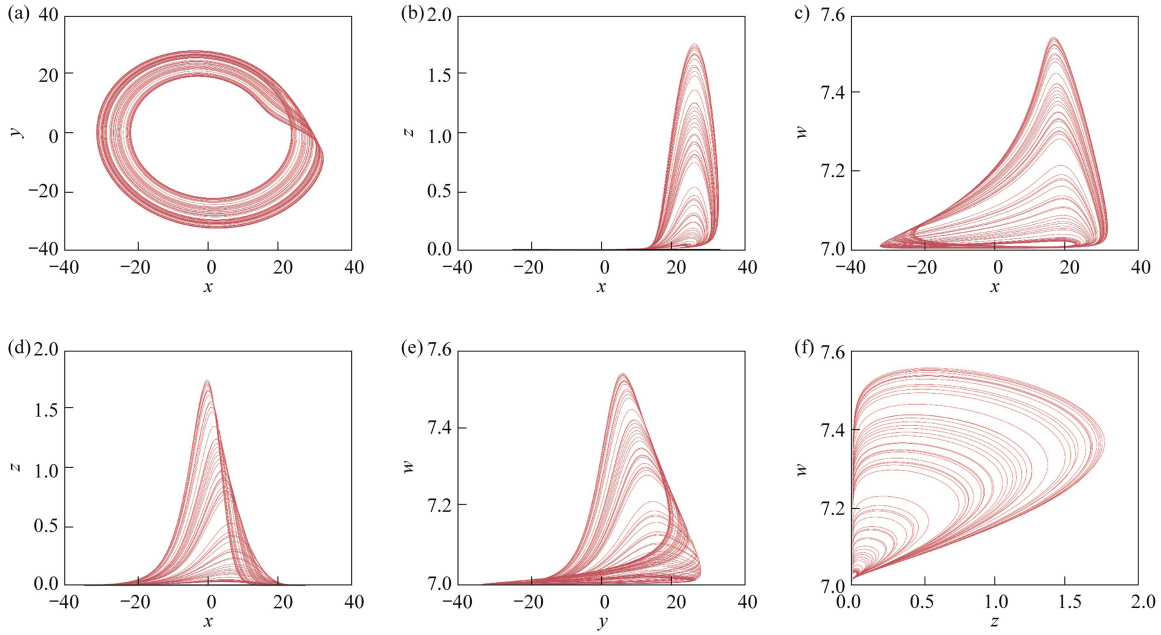

Fig. 6. Phase diagrams of the novel four-dimensional chaotic system (1) when $a = 0.1$, $b = 0.1$, $c = 2.2$, $k_1 = 0.3$, $k_2 = 3.2$, $n = 7$. (a) x–y phase, (b) x–z phase, (c) x–w phase, (d) y–z phase, (e) y–w phase, (f) z–w phase.

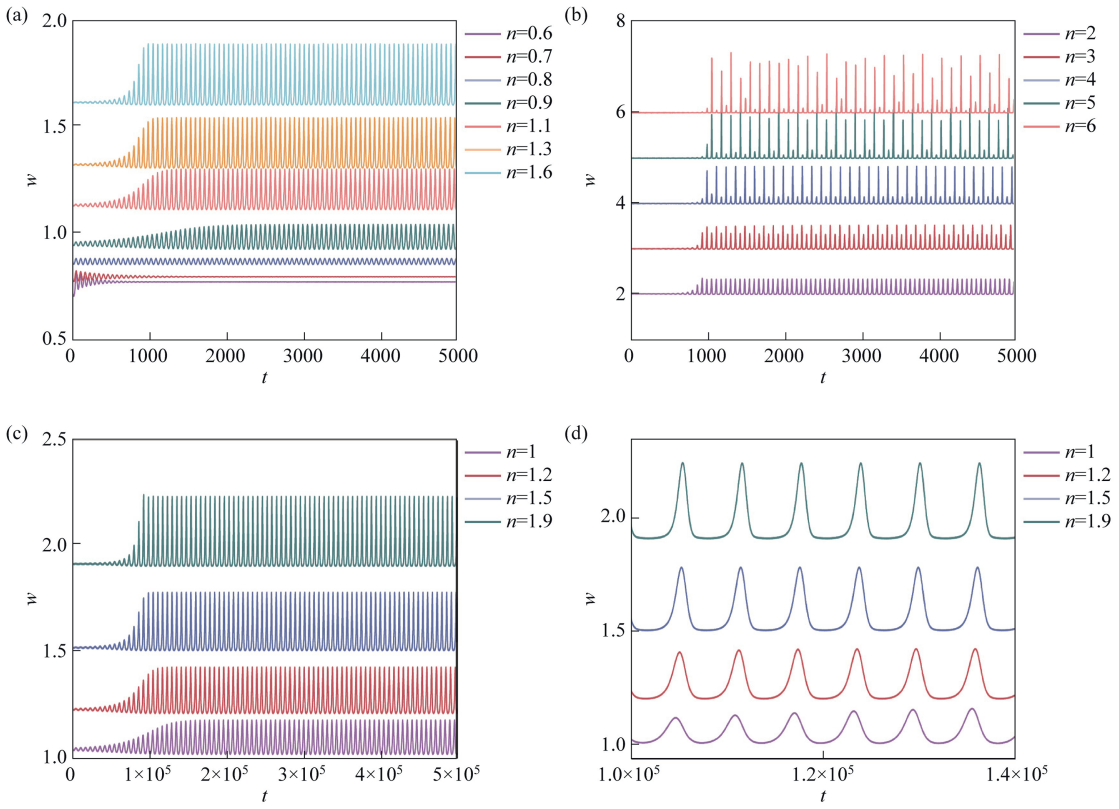

Fig. 7. Signal of the fourth-dimension w of system 1 with $a = 0.1$, $b = 0.1$, $c = 2.2$, $k_1 = 0.3$, $k_2 = 3.2$. (a) $n = 0.6$–1.6, (b) $n = 2$–6, (c) $n = 1$–1.9, (d) enlarged signals of (c).

controlled by the constant n. As the constant n increases, the amplitude of the w signal rises, and concurrently, the offset of the w signal intensifies. However, when the parameter n is adjusted from 2 to 6, the w signal not only experiences an offset but also gradually transitions from a periodic to a chaotic motion state (Fig. 7(b)). Moreover, Fig. 7(c)–(d) further demonstrate that the frequency magnitude of the w signal is governed by the constant n. The more rapidly the constant n increases, the more significant the amplitude of the w signal oscillation becomes. It can be observed that by introducing the constant n, we not only attain synchronous enhancement of the amplitude, frequency, and offset of the w signal, but more importantly, this approach endows the parameter n with the direct ability to control the motion state of the w signal.

Based on the findings in Sections 3.3 and 3.4, we observed that as the external voltage or current increases, the amplitude and frequency of the anodic electrochemical oscillations also increase, accompanied by an offset. When system (1) is used as an electrical circuit, adjusting the parameter n allows for the control of electrical signals with varying amplitudes and frequencies, while also inducing an offset in the signal. This further indicates that it is consistent with the evolutionary law of electrochemical oscillation, and it may have a regulatory effect on anodic electrochemical oscillations, with the potential to predict their behavior. This discovery offers a fresh perspective for the further regulation of anodic electrochemical oscillations and the reduction of electrolysis energy consumption.

4.3. Attractor after phase space reconstruction of w

To more intuitively observe the impact of the parameter n on the state variable w, the delay time method is employed to obtain the attractors of w for $n = 1$ and $n = 7$. Adjusting the delay time τ can alter the shape of the attractor, making it vital to choose the optimal τ to present the most comprehensive information. At $n = 1$, the attractor gradually expands outward from a nearly linear state as τ increases, becoming increasingly clear (Fig. 8(a)–(c)). The optimal delay time is $\tau = 0.3$, which reveals the most complete information. As shown in Fig. 8(d)–(f), the attractor obtained from the phase space reconstruction of w at parameter $n = 7$ exhibits similar changes as the attractors in Fig. 8(a)–(c). By comparing Fig. 8(a)–(c) with Fig. 8(d)–(f), it becomes evident that as the parameter n increases, the shape of the attractor remains largely unchanged for the same delay time, while the motion state of the system changes. It is indicated that the variation of parameter n can influence the state of the system, with outcomes similar to the effect of parameter n on the state variable w in Section 4.2.

4.4. Lyapunov exponents and bifurcation diagram

To explore the impact of parameters n, c, and k_1 on the dynamical state of the system, we calculated the corresponding Lyapunov exponents and bifurcation diagrams using MATLAB. As the bifurcation parameter n increases, the system undergoes successive transitions from chaotic to periodic and back to

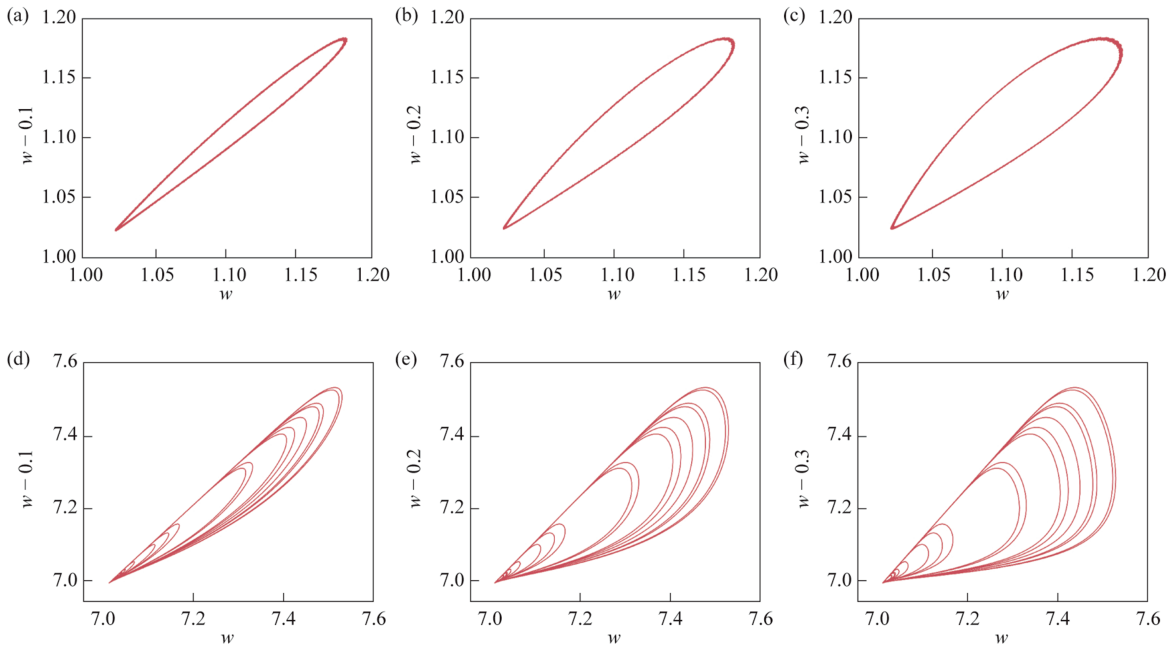

Fig. 8. Delay mapping phase space reconstruction diagram of w. (a)–(c): $a = 0.1$, $b = 0.1$, $c = 2.2$, $k_1 = 0.3$, $k_2 = 3.2$, $n = 1$, (d)–(f): $a = 0.1$, $b = 0.1$, $c = 2.2$, $k_1 = 0.3$, $k_2 = 3.2$, $n = 7$. (a) $\tau = 0.1$, (b) $\tau = 0.2$, (c) $\tau = 0.3$, (d) $\tau = 0.1$, (e) $\tau = 0.2$, (f) $\tau = 0.3$.

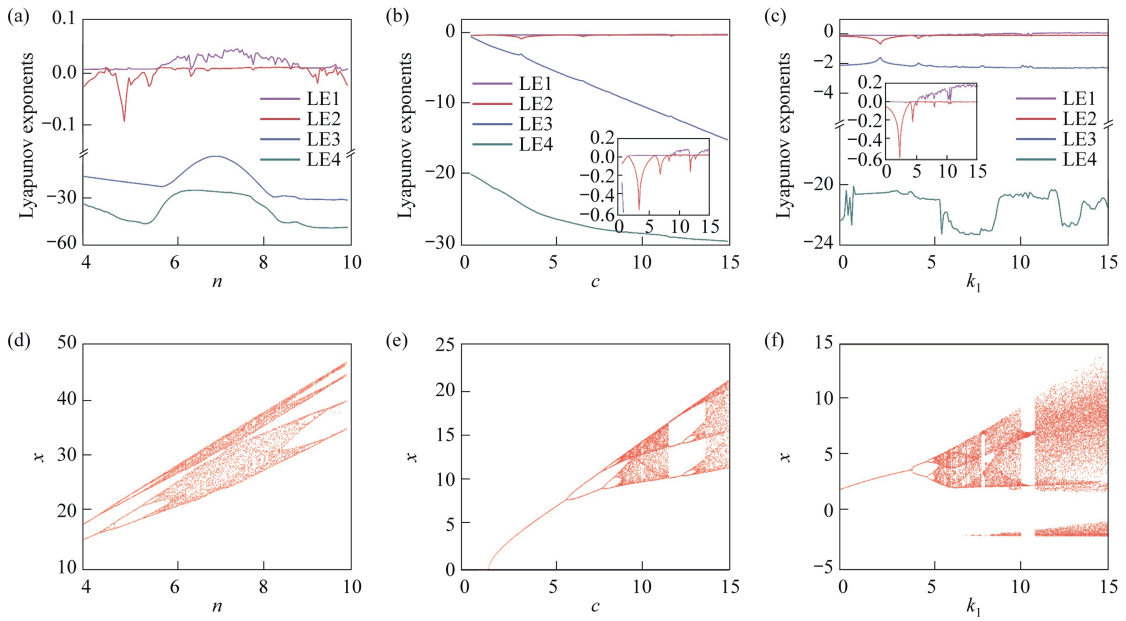

Fig. 9. Lyapunov exponents and bifurcation diagram. (a) The variation of Lyapunov exponents with parameter n when $a = 0.1$, $b = 0.1$, $c = 2.2$, $k_1 = 0.3$, $k_2 = 3.2$, (b) the variation of Lyapunov exponents with parameter c when $a = 0.1$, $b = 0.1$, $k_1 = 0.3$, $k_2 = 3.2$, $n = 1$, (c) the variation of Lyapunov exponents with parameter k_1 when $a = 0.1$, $b = 0.1$, $c = 2.2$, $k_2 = 3.2$, $n = 1$, (d) the corresponding bifurcation diagram with parameter n, (e) The corresponding bifurcation diagram with parameter c, (f) the corresponding bifurcation diagram with parameter k_1.

chaotic states. This dynamic evolution is rigorously supported by the alternation between positive and negative Lyapunov exponents (Fig. 9(a) and (d)). Similarly, as the bifurcation parameter c increases from 0 to 15, the system exhibits successive transitions through 2-cycle, 4-cycle, chaos, 5-cycle, and chaos, which are validated by the corresponding alternations in

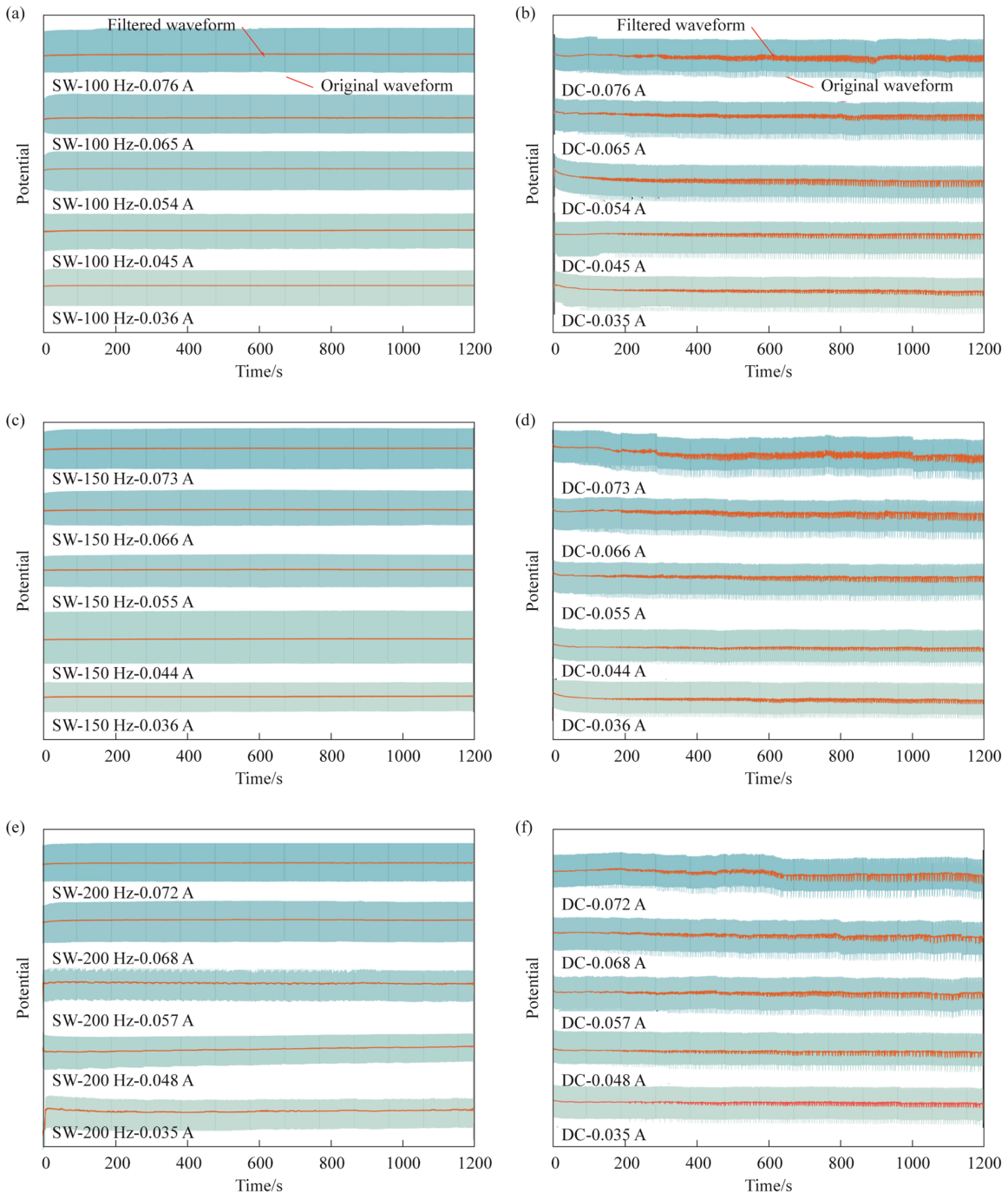

Fig. 10. Comparison of SW electrolysis and DC electrolysis anode potential signals at the same current. (a) SW current frequency of 100 Hz, (b) DC electrolysis potential signal corresponding to (a); (c) SW current frequency of 150 Hz, (d) DC electrolysis potential signal corresponding to (c); (e) SW current frequency of 200 Hz, (f) DC electrolysis potential signal corresponding to (e).

Lyapunov exponents (Fig. 9(b) and (e)). As the bifurcation parameter $k_1$increased from 0 to 15, the system exhibited successive periodic-to-chaotic transitions, with a transient periodic window emerging between two chaotic regimes (Fig. 9(c) and (f)). This bifurcation sequence is quantitatively validated by the corresponding Lyapunov exponent spectrum. The research results show that, with the variation of parameters, the system exhibits a rich variety of states, including stable, periodic, and chaotic states.

5. Square Wave Circuit Application

5.1. Effect of square wave circuit on potential oscillation

To investigate the impact of the SW circuit on the electrochemical oscillation of the anode, the SW circuit was employed in manganese electrolysis experiments. The SW circuit is equipped with capabilities for amplitude modulation, frequency modulation, and signal offset, allowing for the adjustment of output signals at different frequencies to facilitate comparative experiments (Fig. S3). The average current value of SW electrolysis was obtained from the collected current signal, and DC electrolysis used this average value as the output current.

A comparison of Fig. 10(a) and (b) shows that during DC electrolysis, the anode exhibits potential oscillations to varying degrees. However, when a SW circuit is used as the power supply to output electrical signals, the anode potential oscillations are suppressed, with virtually no oscillations observed across the entire current gradient. Subsequently, we investigated the impact of the SW circuit on anode potential oscillations when outputting electrical signals at different frequencies. As illustrated in Fig. 10(c)–(f), the anode potential oscillations remain suppressed across the entire current gradient, consistent with the results obtained when the electrical signal frequency was 100 Hz. As a result, it has been proven that SW circuit can effectively regulate anode potential oscillations to a certain extent. Furthermore, the effective suppression of these oscillations helps to improve the stability of the electrolytic manganese metal production process.

5.2. Effect of square wave circuit on cell voltage and internal resistance of solution

To investigate the impact of the SW electrolysis on the electrolysis cell voltage and solution internal resistance, controlled experiments were carried out using both DC and SW at the same current. As illustrated in Fig. 11(a)–(c), the cell voltage rises as the electrolysis current increases; however, the cell voltage for SW electrolysis is lower than that of DC electrolysis across the entire current range. Specifically, at a signal output frequency of 100 Hz for SW circuit, the cell voltage decreases by an average of 11.39%. At signal output frequencies of 150 Hz and 200 Hz, the average reductions in slot voltage are 11.56% and 12.97%, respectively. Based on the above results, it is concluded that the optimal reduction in slot voltage is achieved at a signal output frequency of 200 Hz.

The solution internal resistance is calculated based on the cell voltage and output current. As illustrated in Fig. 11(d)–(f), the solution internal resistance of SW electrolysis remains lower than that of DC electrolysis throughout the entire current range as the output current of the power supply increases. This suggests an increase in the ion migration rate within the solution, which leads to an accelerated reaction rate and a gradual decrease in the solution's internal resistance. Specifically, at a signal output frequency of 100 Hz for the SW current, the solution internal resistance decreases by an average of 11.20%. As the frequency rises

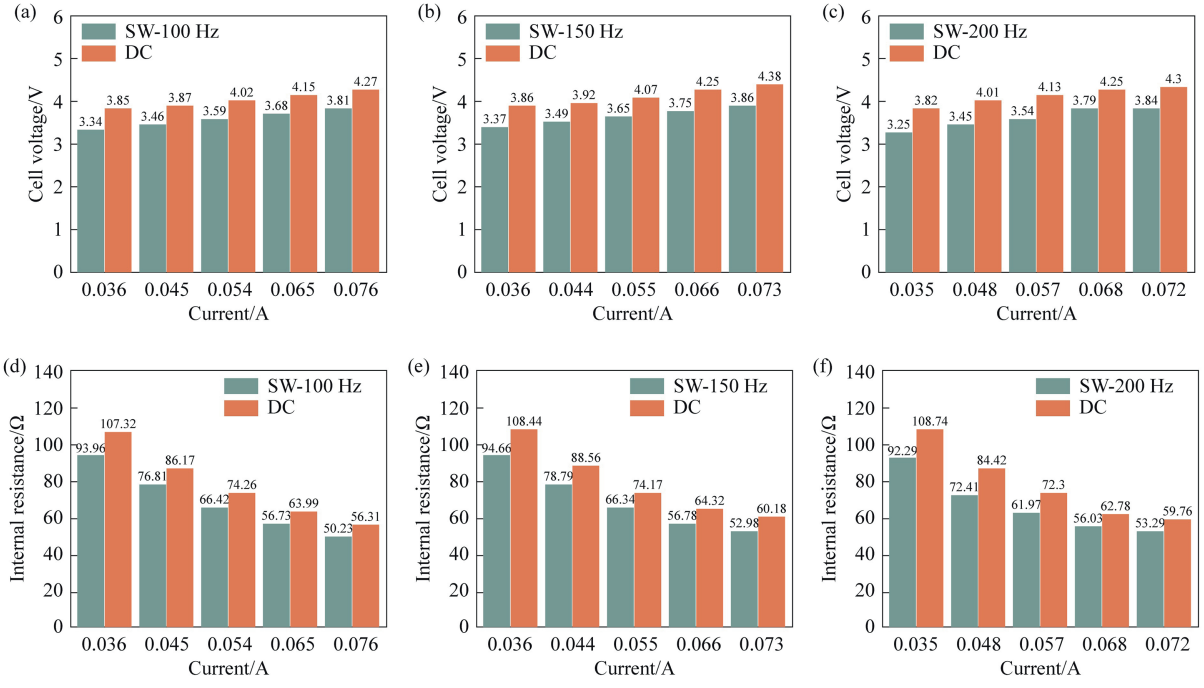

Fig. 11. Comparison of SW and DC cell voltages and solution internal resistance at the same current. Cell voltage comparison with (a) 100 Hz, (b) 150 Hz, (c) 200 Hz frequency; internal resistance comparison with (d) 100 Hz, (e) 150 Hz, (f) 200 Hz frequency.

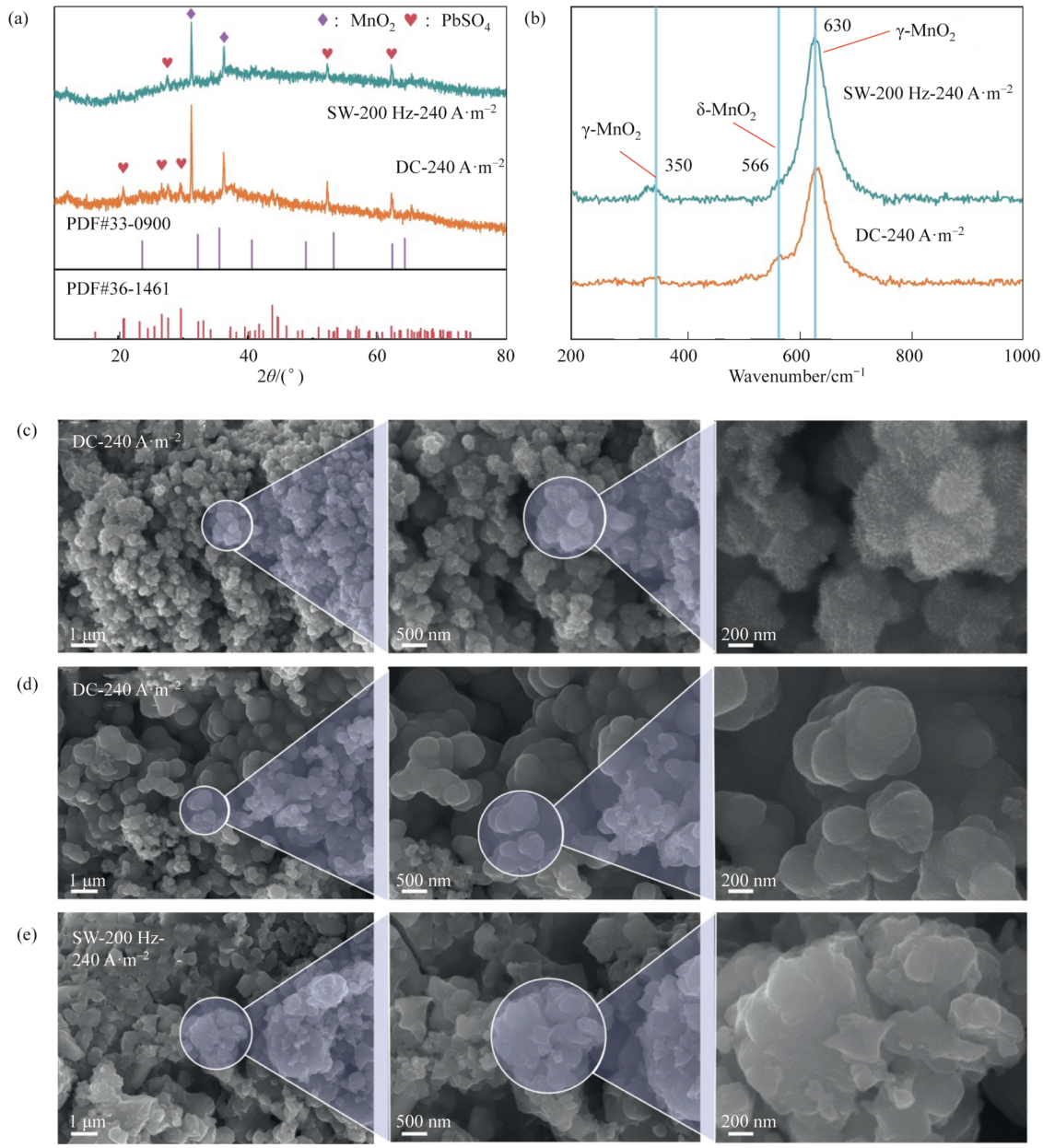

Fig. 12. Microstructure and phase composition analysis of anode products. (a) XRD analysis of anode products; (b) Raman analysis of anode products; (c) and (d) microstructure of anode products under DC electrolysis; (e) microstructure of anode products under SW electrolysis.

to 150 Hz and then to 200 Hz, the average reduction in solution internal resistance reaches 11.59% and 13.04%, respectively. Based on the aforementioned results, it is evident that the optimal electrical signal output frequency is 200 Hz. It is evident that the SW circuit markedly lowers the cell voltage and solution internal resistance, thus offering an effective approach for reducing the energy consumption in electrolytic manganese production. This holds great significance for achieving energy savings and emission reductions in the electrolytic manganese industry.

5.3. *Effect of square wave circuit on anode slime*

To explore the impact of the SW circuit on the anode deposits, the anode deposits from both the SW and DC electrolysis were characterized and tested separately. XRD analysis revealed that the primary components of the anode deposits consisted of MnO_2 and $PbSO_4$ (Fig. 12(a)). The Raman spectra exhibited characteristic peaks for γ-MnO_2 at 350 cm^{-1} and 630 cm^{-1} [56,57], as well as for δ-MnO_2 at 566 cm^{-1} [58], indicating the presence of two distinct MnO_2 crystal types in the anode deposits (Fig. 12(b)). SEM images revealed that the anodic deposits from DC electrolysis primarily consisted of MnO_2 spherical particles that gradually accumulated. Furthermore, it was observed that there were two distinct types of MnO_2 spherical particles under DC electrolysis: one type was covered with needle-like protrusions on its surface, while the other exhibited a smooth surface (Fig. 12(c)–(d)). In comparison to the DC electrolysis anode deposit, the anodic deposit

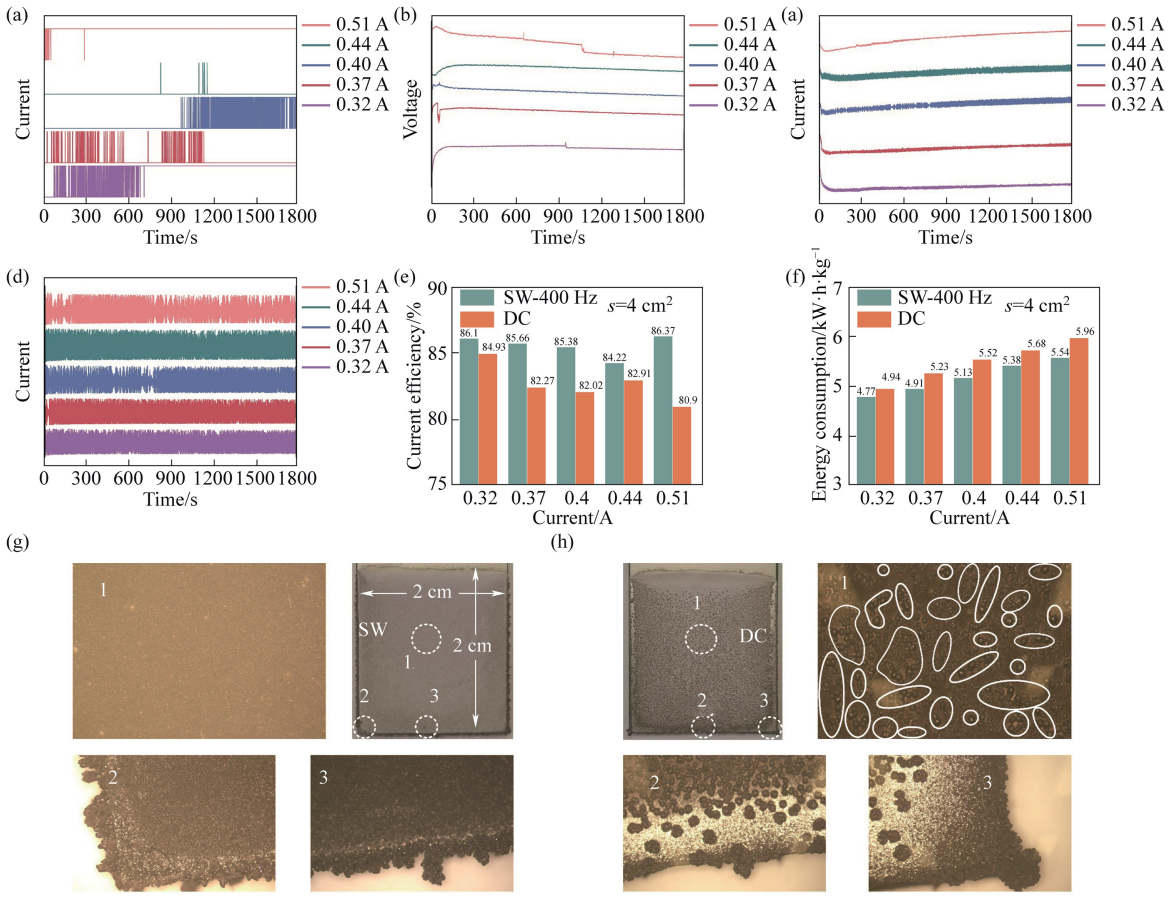

Fig. 13. Comparison of signals, current efficiency, energy consumption and deposits in different electrolytic processes after 30 min of electrolysis (SW:400 Hz). (a) DC current signal; (b) DC voltage signal; (c) SW current signal; (d) SW voltage signal; (e) current efficiency; (f) energy consumption; (g) SW deposits; (h) DC deposits.

from SW electrolysis also formed through stacking, but it was composed of irregular, lumpy particles (Fig. 12(e)). Based on this, we speculate that SW current influences the formation of anode slime by generating MnO_2 particles with different structures, thereby regulating the anode potential oscillations.

5.4. Effect of square wave circuits on current efficiency and energy consumption

To verify the advantage of SW current in reducing energy consumption during manganese electrodeposition, manganese metal electrodeposition experiments were conducted under simulated industrial conditions (Electrolysis time: 30 min). During electrolysis, current and voltage fluctuations within a certain range were observed for both DC and SW electrolysis (Fig. 13(a)–(d)). Therefore, the current and voltage throughout the entire process were collected, and their average values were used to calculate current efficiency and energy consumption. Comparative analysis demonstrated that SW electrolysis (400 Hz) exhibited significantly superior current efficiency than DC electrolysis over a wide current range, with an average enhancement of 3.6% (Fig. 13 (e) and Table S1). In terms of energy consumption, SW electrolysis also displayed significantly reduced values, averaging 0.32 $kW \cdot h \cdot kg^{-1}$ less than DC electrolysis (Fig. 13(f) and Table S1). The surface morphology of cathodic metallic manganese is presented in Fig. 13(g)–(h). Optical microscopy analysis demonstrated the absence of spherical dendrites in the central regions of the SW-electrodeposited layers, with only limited dendritic growth observed at the electrode edges. Similar observations were consistently noted in deposited layers formed under different applied currents (Fig.S4).

The surface morphology of cathodic manganese deposits after 30 min of electrolysis is shown in Fig. 14. Under SW current, the manganese surface is dominated by irregular prismatic cone structures, whereas DC generates spherical dendrites with non-uniform sizes on the deposited surface (Fig. 14(a) and (b)). The dendritic growth of manganese on cathodes primarily originates from non-uniform current density distribution across the electrode. Specifically, the current density at the cathode plate edges typically exceeds that at the central regions, promoting preferential dendrite formation along the periphery. Such dendritic structures not only risk inducing short circuits between electrodes but also reduce current efficiency. Notably, the effective suppression of dendritic growth using SW current highlights its role in optimizing current density distribution (Fig. 14(c) and (d)). This work proposes a novel strategy to alleviate inter-electrode short-circuiting induced by dendrite formation in industrial electrolytic manganese production.

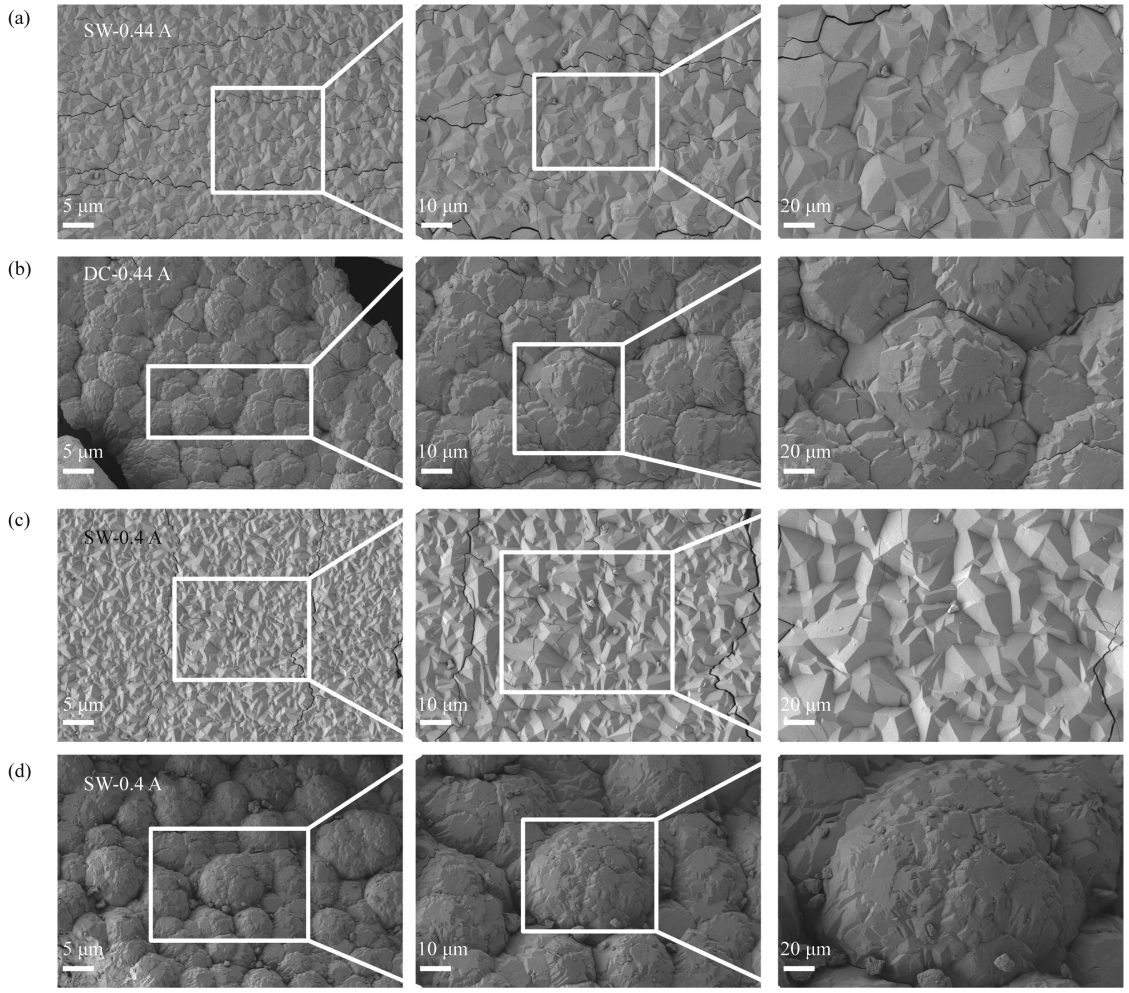

Fig. 14. SEM image of cathodic manganese metal after 30 min of electrolysis. (a) Average SW current: 0.44 A; (b) average DC current: 0.44 A; (c) average SW current: 0.40 A; (d) average DC current: 0.40 A.

6. Conclusions

In this study, the analysis of the electrochemical signals at the anode revealed that, although the evolutionary laws of the current and potential oscillation signals were consistent, the waveform structures of the oscillations exhibited opposite directions. Furthermore, as the current density increases, the electrochemical oscillation signals shift towards higher current and potential values, with a simultaneous increase in amplitude and frequency.

To achieve more effective regulation of electrochemical oscillation signals, we independently designed a frequency-adjustable SW circuit and successfully applied it in the electrolysis of manganese metal. The experimental results demonstrated that the SW current effectively suppressed both electrochemical oscillations and the growth of manganese dendrites. Furthermore, compared to direct current electrolysis, the SW current improved the current efficiency by 3.6% and reduced the energy consumption by 0.32 $kW \cdot h \cdot kg^{-1}$.

To gain a clearer and deeper understanding of the evolution law of electrochemical oscillations, we proposed a novel four-dimensional chaotic system based on experimental results. The evolution of its amplitude and frequency with varying parameters closely matched the experimental observations. By adjusting the parameter n, we could control the output of electrical signals with different amplitudes or frequencies, which also exhibited shifts. This provided a theoretical reference for the process of electrochemical oscillation reactions.

The newly designed SW circuit in this study not only opens up a novel pathway for reducing energy consumption in the electrolytic manganese industry but also provides valuable theoretical and technical references for other electrolytic industries and their process improvements.

CRediT Authorship Contribution Statement

Jiaxing Li: Writing – original draft. Chunbiao Li: Investigation. Jie Yang: Methodology. Zhihao Wu: Data curation. Qian Zhang: Data curation. Guocan Zheng: Conceptualization, Project administration. Zuohua Liu: Funding acquisition. Changyuan Tao: Conceptualization.

Declaration of Competing Interest

The authors declare that they have no known competing financial interests or personal relationships that could have appeared to influence the work reported in this paper.

Acknowledgements

The financial support from the Fundamental Research Funds for the Central Universities (2022CDJQY-005, 2024CDJXY010) and the Guangxi Science and Technology Program (AB24010229) is greatly acknowledged.

Supplementary Material

Supplementary data to this article can be found online at https://doi.org/10.1016/j.cjche.2025.07.022.

References

[1] A. Chakraborty, P. Veeresha, Effects of global warming, time delay and chaos control on the dynamics of a chaotic atmospheric propagation model within the frame of Caputo fractional operator, *Commun. Nonlinear Sci. Numer. Simul.* 128 (2024) 107657.
[2] I. Bashkirtseva, L. Ryashko, T. Ryazanova, Stochastic variability and transitions to chaos in a hierarchical three-species population model, *Chaos Solitons Fractals* 119 (2019) 276–328.
[3] A.I. Kakkassery, V.J. Rajesh, R.K. Sinha, D. Padmakumar, K.S. Sajinkumar, Evolutionary history of western Eos chaos of valles marineris, Mars: insights from morphological characteristics, *Geosyst. Geoenviron.* 2 (4) (2023) 100207.
[4] E.N. Lorenz, Deterministic nonperiodic flow, *J. Atmos. Sci.* 20 (2) (1963) 130–141.
[5] Z.Y. Zhong, W. Lin, B.W. Qin, Modulating biological rhythms: a non-computational strategy harnessing nonlinearity and decoupling frequency and amplitude, *Phys. Rev. Lett.* 131 (13) (2023) 138401.
[6] X.X. Peng, S.J. Zhou, Finite-time stochastic control for complex dynamical systems: the estimate for control time and energy consumption, *Syst. Control Lett.* 184 (2024) 105711.
[7] G.Z. Hu, B.B. Li, Coupling chaotic system based on unit transform and its applications in image encryption, *Signal Process.* 178 (2021) 107790.
[8] N. Khalil, A. Sarhan, M.A.M. Alshewimy, An efficient color/grayscale image encryption scheme based on hybrid chaotic maps, *Opt. Laser Technol.* 143 (2021) 107326.
[9] S.K. Yang, C.L. Chen, H.T. Yau, Control of chaos in Lorenz system, *Chaos Solitons Fractals* 13 (4) (2002) 767–780.
[10] R. Martínez-Guerra, J.L. Mata-Machuca, Generalized synchronization *via* the differential primitive element, *Appl. Math. Comput.* 232 (2014) 848–857.
[11] R.B. Wafo Tekam, J. Kengne, G. Djuidje Kenmoe, High frequency colpitts' oscillator: a simple configuration for chaos generation, *Chaos Solitons Fractals* 126 (2019) 351–360.
[12] J.F. Chang, M.L. Hung, Y.S. Yang, T.L. Liao, J.J. Yan, Controlling chaos of the family of Rössler systems using sliding mode control, *Chaos Solitons Fractals* 37 (2) (2008) 609–616.
[13] O.S. Ojoniyi, A.N. Njah, A 5D hyperchaotic Sprott B system with coexisting hidden attractors, *Chaos Solitons Fractals* 87 (2016) 172–181.
[14] J. Zhang, J.Y. Hou, L.H. Xu, X.P. Zhu, Q.G. Xie, Dynamical analysis, circuit implementation, and simultaneous application of a novel four-dimensional hyperchaotic system based on cosine functions, *Microelectron. Eng.* 271 (2023) 111939.
[15] J.B. Wang, R. Zhang, J.K. Liu, J. Li, Control of Hopf bifurcation for a four-dimensional fractional order hyperchaotic system with coexisting attractors, *Nonlinear Dyn.* 112 (22) (2024) 20401–20415.
[16] C.B. Xiu, J.Y. Fang, Y.X. Liu, Design and circuit implementation of a novel 5D memristive CNN hyperchaotic system, *Chaos Solitons Fractals* 158 (2022) 112040.
[17] Z.B. Guo, J.H. Ma, The influence of information acquisition on the complex dynamics of market competition, *Int. J. Bifurcation Chaos* 26 (1) (2016) 1650008.
[18] H. Yo, Discontinuity-induced bifurcations and chaos in a linear ring oscillator with a piecewise linear reverse coupling, *Int. J. Bifurcation Chaos* 33 (14) (2023) 2330035.
[19] W.R. Lv, J.X. Chen, Q.K. Li, X. Xu, C. Fu, An efficient medical image encryption scheme utilizing nonuniform cellular automaton, *Int. J. Bifurcation Chaos* 33 (10) (2023) 2350119.
[20] A.H. Tian, C.B. Fu, H.G. Xiong, H.T. Yau, Innovative intelligent methodology for the classification of soil salinization degree using a fractional-order master-slave chaotic system, *Int. J. Bifurcation Chaos* 29 (2) (2019) 1950026.
[21] L. Xiong, F.F. Yang, X.L. An, X.G. Zhang, Hyperchaotic system with application to image encryption, *Int. J. Bifurcation Chaos* 32 (13) (2022) 2250191.
[22] W.L. Li, H.X. Jin, H.Y. Xie, L.R. Ma, Synthesis of zeolite A and zeolite X from electrolytic manganese residue, its characterization and performance for the removal of Cd^{2+} from wastewater, *Chin. J. Chem. Eng.* 62 (2023) 31–45.
[23] J.C. Shu, X.F. Zeng, D.Y. Sun, Y. Yang, Z.H. Liu, M.J. Chen, D.Y. Tan, Enhanced Mn^{2+} solidification and NH_4^+-N removal from electrolytic manganese metal residue *via* surfactants, *Chin. J. Chem. Eng.* 49 (2022) 205–221.
[24] D. Sun, L. Yang, N. Liu, W.J. Jiang, X. Jiang, J.J. Li, Z.Y. Yang, Z.P. Song, Sulfur resource recovery based on electrolytic manganese residue calcination and manganese oxide ore desulfurization for the clean production of electrolytic manganese, *Chin. J. Chem. Eng.* 28 (3) (2020) 864–870.
[25] T.Y. Zhang, J.C. Shu, M.J. Chen, L. Wei, Y. Yang, Recovery and utilization of electrolytic manganese anode slime for the high-value industrialized products-a review, *Ind. Eng. Chem. Res.* 62 (33) (2023) 12703–12715.
[26] K.A. Gebru, C. Das, Effects of solubility parameter differences among PEG, PVP and CA on the preparation of ultrafiltration membranes: impacts of solvents and additives on morphology, permeability and fouling performances, *Chin. J. Chem. Eng.* 25 (7) (2017) 911–919.
[27] N.K. Onkarappa, P.S. Adarakatti, P. Malingappa, A study on the effect of additive combination on improving anticorrosion property of zinc electrodeposit from acid chloride bath, *Ind. Eng. Chem. Res.* 56 (18) (2017) 5284–5295.
[28] Y.Q. Wang, X. Wang, P. Gao, J.C. Jiang, A.C. Huang, Novel composite electrolyte additive for enhancing the thermal and cycling stability of SiO/C anode Li-ion battery, *Process Saf. Environ. Prot.* 189 (2024) 756–767.
[29] Y.Q. Wang, L.J. Xie, H.Q. Sun, X. Wang, H.L. Zhou, Y. Tang, J.C. Jiang, A.C. Huang, 4, 5-Difluoro-1, 3-dioxolan-2-one as a film-forming additive improves the cycling and thermal stability of SiO/C anode Li-ion batteries, *Process Saf. Environ. Prot.* 183 (2024) 496–504.
[30] Z.H. Wu, Y. Wu, Y. Tang, J.C. Jiang, A.C. Huang, Evaluation of composite flame-retardant electrolyte additives improvement on the safety performance of lithium-ion batteries, *Process Saf. Environ. Prot.* 169 (2023) 285–329.
[31] C.W. Zhao, X.N. Wang, J.S. He, Y.Y. Wang, Z.K. Luan, Effect of polyethylene glycol on the properties of γ-Al_2O_3 formation by polyaluminum chloride, *Chin. J. Chem. Eng.* 20 (5) (2012) 1034–1038.
[32] Y.H. Cheng, H. Guo, Interface modification of electrodes through polyethylene glycol in rechargeable zinc-nickel batteries, *Chem. Eng. Sci.* 232 (2021) 11637.
[33] J.M. Lu, D. Dreisinger, T. Glück, Electrolytic manganese metal production from manganese carbonate precipitate, *Hydrometallurgy* 161 (2016) 45–55.
[34] J. Yang, C.B. Li, Q. Zhang, X. Zhang, Z.H. Wu, H.D. Zhong, P.Q. Liu, Z.H. Liu, C.Y. Tao, K.Y. Huang, J.X. Li, G.C. Zheng, A memristive hyperchaotic oscillator with complete control and its application in the electrolysis of manganese, *Chaos Solitons Fractals* 183 (2024) 1148.
[35] Z.N. Xie, Z.H. Liu, C.Y. Tao, C.B. Li, J. Chang, Production of electrolytic manganese metal using a new hyperchaotic circuit system, *J. Mater. Res. Technol.* 18 (2022) 4804–4815.
[36] F. Hakimi, F. Rashchi, M. Ghalekhani, A. Dolati, F. Razi Astaraei, Effect of a synthesized pulsed electrodeposited Ti/PbO_2–RuO_2 nanocomposite on zinc electrowinning, *Ind. Eng. Chem. Res.* 60 (31) (2021) 11737–11748.
[37] N.K. Jain, S. Pathak, M. Alam, Synthesis of copper nanoparticles by pulsed electrochemical dissolution process, *Ind. Eng. Chem. Res.* 58 (2) (2019) 602–608.
[38] M. Hansen, P.R. Protachevicz, K.C. Iarosz, I.L. Caldas, A.M. Batista, E.E.N. Macau, Dynamics of uncoupled and coupled neurons under an external pulsed current, *Chaos Solitons Fractals* 155 (2022) 111734.
[39] Y.X. Gao, Y. Zhou, H.T. Wang, W.S. Lin, Y.P. Wang, D.H. Sun, J.Q. Hong, Q.B. Li, Simultaneous silver recovery and cyanide removal from electroplating wastewater by pulse current electrolysis using static cylinder electrodes, *Ind. Eng. Chem. Res.* 52 (17) (2013) 5871–5879.
[40] P. Ruiz, J.M. Gutiérrez, J. Güémez, Experimental mastering of nonlinear dynamics in circuits by sporadic pulses, *Chaos Solitons Fractals* 36 (3) (2008) 635–645.
[41] Q.Z. Wan, F. Li, S.M. Chen, Q. Yang, Symmetric multi-scroll attractors in magnetized Hopfield neural network under pulse controlled memristor and pulse current stimulation, *Chaos Solitons Fractals* 169 (2023) 113259.
[42] F. Jafari, J. Saien, Experimental and model study for liquid–liquid extraction of conductive nanofluid drops under low voltage pulsed electric fields, *Chem. Eng. Sci.* 258 (2022) 11776.
[43] H.F. Gong, Z.X. Liao, Y. Peng, Z. Qiu, B. Yu, Y.Y. Zhang, Numerical simulation of dynamic characteristics of droplet in oil under a CPPM electric field, *Chem. Eng. Sci.* 248 (2022) 117248.
[44] Q.F. Wei, X.L. Ren, J. Du, S.J. Wei, S.R. Hu, Study of the electrodeposition conditions of metallic manganese in an electrolytic membrane reactor, *Miner. Eng.* 23 (7) (2010) 578–586.
[45] X. Fan, D.P. Yang, L.F. Ding, J. Du, C.Y. Tao, Periodic current oscillation catalyzed by δ-MnO_2 nanosheets, *ChemPhysChem* 16 (1) (2015) 176–180.
[46] J.M. Lu, D. Dreisinger, T. Glück, Manganese electrodeposition: a literature review, *Hydrometallurgy* 141 (2014) 105–116.
[47] G. Buzsáki, A. Draguhn, Neuronal oscillations in cortical networks, *Science* 304 (5679) (2004) 1926–1929.
[48] H.X. Wang, Q.Y. Wang, Q.S. Lu, Bursting oscillations, bifurcation and synchronization in neuronal systems, *Chaos Solitons Fractals* 44 (8) (2011) 667–675.
[49] X. Fan, J. Hou, D.G. Sun, S.Y. Xi, Z.H. Liu, J. Du, J.L. Luo, C.Y. Tao, Mn-oxides catalyzed periodic current oscillation on the anode, *Electrochim. Acta* 102 (2013) 466–471.
[50] D. Rand, L.S. Young, Dynamical Systems and Turbulence, Warwick 1980, Springer Berlin Heidelberg, 1981.
[51] V. Dakos, M. Scheffer, E.H. van Nes, V. Brovkin, V. Petoukhov, H. Held, Slowing down as an early warning signal for abrupt climate change, *Proc. Natl. Acad. Sci. USA* 105 (38) (2008) 14308–14311.
[52] T.M. Lenton, Early warning of climate tipping points, *Nat. Clim. Change* 1 (4) (2011) 201–209.

[53] G. Sugihara, R. May, H. Ye, C.H. Hsieh, E. Deyle, M. Fogarty, S. Munch, Detecting causality in complex ecosystems, *Science* 338 (6106) (2012) 496–500.
[54] X.P. Yan, Q. Hu, L. Teng, Y.N. Su, Unmanned ship image encryption method based on a new four-wing three-dimensional chaotic system and compressed sensing, *Chaos Solitons Fractals* 185 (2024) 115146.
[55] T.K. Zhao, X. Sun, Z.Y. Fan, B.X. Du, A new two-parameter controllable multi-scroll 4D Hamiltonian conservative hyperchaotic system with improved nested COS-PWL function, *Chaos Solitons Fractals* 189 (2024) 115585.
[56] C. Julien, M. Massot, S. Rangan, M. Lemal, D. Guyomard, Study of structural defects in γ-MnO_2 by Raman spectroscopy, *J. Raman Spectrosc.* 33 (4) (2002) 223–228.
[57] J. Yang, C.B. Li, Q. Zhang, H.D. Zhong, Z.H. Wu, P.Q. Liu, Z.H. Liu, K.Y. Huang, C. Y. Tao, G.C. Zheng, Y. Yang, H.K. Wei, Hyperchaotic power with wide current variation for efficient manganese electrodeposition, *Chem. Eng. Sci.* 293 (2024) 120010.
[58] Y. Chen, C.Z. Lin, X. Chen, Z.H. Lu, K.C. Zhang, Y. Liu, J.N. Wang, G.R. Han, G. Xu, Modulating the structure of interlayer/layer matrix on δ-MnO_2 *via* cerium doping-engineering toward high-performance aqueous zinc ion batteries, *Adv. Energy Mater.* 14 (35) (2024) 230430.